Fabrication of a Curved-Canted-Cosine-Theta (CCCT) Dipole at CERN

Ariel Haziot, Alessandro Dallocchio, Arnaud Devred, *Senior Member, IEEE*, Luca Gentini, Glyn Kirby, Mariano Pentella, Carlo Petrone, Francois-Olivier Pincot, Jean-Sébastien Rigaud, and Jorge Guardia-Valenzuela

***Abstract*—Canted Cosine Theta (CCT) magnet is an interesting design for compact accelerators or gantry systems for hadron-therapy. It offers great flexibility in generating complex field harmonics in straight and curved configurations while remaining compact. The Fusillo project based at CERN aims to design, build, and test a Nb-Ti curved CCT dipole demonstrator generating 3 T at 4.5 K in a large aperture of 236 mm, bent over 90° with a small bending radius of 1 m, and multi-harmonic field features to correct for the curvature. In this paper, we describe the fabrication process, the winding and the assembly of a Fusillo demonstrator that at present is being cold tested in liquid helium.**

***Index Terms*—Canted-Cosine-Theta (CCT), curved dipole magnet, magnet design, superconducting dipole magnet.**

I. Introduction

Canted Cosine-Theta (CCT) magnets have emerged as a promising solution for compact and high-performance accelerator applications, including medical systems such as ion therapy gantries and isotope production rings. The CCT design, based on two nested tilted solenoids with opposing angles, generates a perfect dipole field with low structural complexity. Originally presented in the 1970 s and proposed in the 2000s as a path towards 20 T dipoles [1], [2], [3], CCT magnets are now being explored in curved configurations to meet the needs of space-constrained systems [4], [5], [6], [7], [8].

The Fusillo project at CERN aims to demonstrate the feasibility of a strongly curved CCT dipole magnet, spanning 90° over a 1 m radius with a 236 mm aperture diameter and a central field of 3.00 T. Developed originally for applications like the HIE-ISOLDE Recoil Separator Ring [9], the magnet design draws on prior experience from the HL-LHC orbit correctors and the LBNL prototype [6], [10].

Prior publications, related to the Fusillo project have detailed the electromagnetic and engineering designs as well as the quench protection of the demonstrator and the fabrication and test results of subscale models [11], [12], [13], [14]. This paper focuses on the fabrication and assembly of the full-size demonstrator magnet.

Received 21 July 2025; revised 17 September 2025; accepted 23 September 2025. Date of publication 8 October 2025; date of current version 16 October 2025. *(Corresponding author: Ariel Haziot.)*

The authors are with the CERN, CH-1211 Meyrin, Switzerland (e-mail: ariel.haziot@cern.ch).

Color versions of one or more figures in this article are available at https://doi.org/10.1109/TASC.2025.3615556.

Digital Object Identifier 10.1109/TASC.2025.3615556

TABLE I
Overview of Fusillo Parameters

Parameter	Unit	Value
Conductor Properties		
Conductor type		Nb-Ti
Cu:non-Cu		1.95
Wire diameter	[mm]	0.825
Wire TPI insulation thickness	[μm]	80
Type of cable		Rope, 6 around 1
Twist pitch	[mm]	45
Raw cable diameter	[mm]	2.96
Cable S2 glass insulation thickness	[μm]	100
Insulated cable diameter	[mm]	3.15
Required length (inner / outer)	[m]	907 / 973
Magnet Properties		
Aperture diameter	[mm]	236
Curvature radius	[m]	1.0
Physical bend / length	[° / m]	94 / 1.65
Number of wire turns		70
Number of winding turns		65
Pitch	[mm]	15.5
Tilt angle* of inner / outer layer	[°]	62.2 / 58.5
Tapering (on the radius)	[mm]	5
Spar thickness on inner / outer former	[mm]	7.0 / 5.3
Channel dimensions	[mm]	17.10×5.88
Minimum rib thickness (mid-plane)	[mm]	1.0
Radial insulation between layers	[mm]	0.6
Radial insulation toward clamshell	[mm]	0.95
Total weight	[kg]	1200
Operation		
Nominal current	[A]	287.5
Bore / Peak field at I_{nom}	[T]	3.0 / 3.6
Field integral in the centre over 90°	[Tm]	2.98
Magnetic bend / length	[° / m]	90 / 1.57
Margin on the load line	[%]	33
Operating temperature	[K]	4.5
Inductance	[H]	9.4
Stored energy	[kJ]	391

* The tilt angle is given from the midplane.

After a brief summary of the magnet parameters and design in Section II, the fabrication of the demonstrator is detailed in Section III. Finally, Section IV describes the instrumentation implemented for the cold tests.

II. Design Summary

The full design optimisation and description are detailed in [11]. Only the main aspects are recalled in Table I for the conductor, coil, and operating parameters.

The conductor relies on Nb-Ti strands, each insulated with a 80 μm thermoplastic (TPI) layer extruded around the wire.

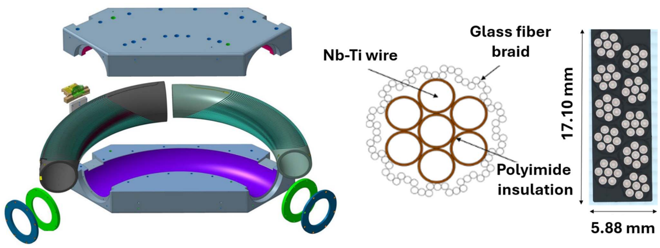

Fig. 1. CAD view of the main parts of the magnet (left). Layout of the rope cable used in Fusillo (centre). Picture of a cross section of a channel with the conductor (right). Both single wires at corners are for instrumentation.

The insulation electrical resistance was measured in water at 20°C under 2 kV at 886±47 GΩ and it remains unchanged after 10 thermal cycles at 77 K. Seven strands are assembled into ropes using a 6-around-1 configuration. Each rope is further insulated with a glass fibre braid to enhance mechanical stability and improve resin impregnation. A total of ten ropes (70 strands connected in series) forms the conductor used in this magnet, as illustrated in Fig. 1.

As is standard for CCT magnets, the conductor is placed within grooves machined into the two nested formers (inner and outer), these define the helical winding path and thereby shape the magnetic field. The target bore field of 3 T is achieved by powering each strand with 287.5 A. The formers are mechanically supported by a structure composed of two half-clamshell elements. Longitudinal constraint is provided by two end flanges that secure the formers within the mechanical assembly. All components, except for the insulating rings, are made from Aluminium 6082 T6, as shown in Fig. 1.

III. Fabrication

A. Formers fabrication

The formers are machined from extruded aluminium alloy EN AW-6082 T6. This alloy was chosen for its higher yield strength at low temperatures compare to other alloys, and its lower electrical resistivity measured at 8.3±3 n$\Omega.m$ at 7 K, 2–3 times below other alloy, thus promoting the generation of eddy currents beneficial for magnet protection. The formers represent one of the most technically demanding components to produce. Each former includes a precision-machined groove with a cross-sectional dimensional tolerance and a positioning of ± 0.05 mm. In addition to being curved, the formers are also tapered, with both the inner and outer surfaces required to meet a global shape tolerance of ±0.2 mm.

The pronounced 90° bend of the component prevents continuous machining of the inner surfaces due to interference between the large cutting tool and the limited bore diameter. Among various solutions—such as the cold-fitting of pre-machined 10° slices used at LBNL [5]—our chosen strategy was to construct each former from three segments of different angles (25°–30°–35°) to avoid the superposition of the joint between the layers. Each segment is machined individually from an aluminium rod, with inner surface and sides operations completed prior to assembly. The joining technique, detailed in [11], involves the injection of Stycast EE4215 epoxy into an orbital slit with a custom-designed geometry located at the segment ends. Stycast EE4215 has been chosen for its mechanical strength, as once cured, it acts as a mechanical pin, creating a robust joint. The separation resistance to traction perpendicular to the joint in a straight mock-up was measured higher than 40 kN [11]. During assembly, the three segments are precisely positioned using reference surfaces, as illustrated in Fig. 2. Following the assembly, the outer surface of the former, including the groove, is re-machined in two stages (top and bottom), as shown in Fig. 2. A custom-made milling bit was used to machine the groove, ensuring accurate groove cross-sectional geometry, and compliance with the global shape tolerances of the former. Final metrology measurements confirmed that geometrical deviations from the ideal shape remained within ± 0.2 mm in 95% of the areas with exceptions at + 0.4 mm at the ends. However, this did not block the insertion thanks to a global elasticity over the full length.

Fig. 2. Assembly of the 3 segments for the inner former, preparing for injection (top). Completed machining of the top outer surface of the assembled former (bottom).

B. Winding

The winding of the formers was performed on a dedicated winding machine capable of independently loading and controlling the tension of ten spools of rope cable. However, in order not to introduce methods not validated through the subscale programme, no tension was applied during winding. A specialised hand tool was used to group the ten ropes together and accurately

Fig. 3. Winding of the inner layer (top). Outer layer finished with the polyimide ground insulation (bottom).

position them according to the groove geometry. As the former rotated, the rope bundle was pushed into the groove (see Fig. 3). 100 μm of clearance in the groove, combined with rounded corners, facilitated smooth insertion of the conductor without damaging the insulation. The conductor was tested during winding against short circuits every five turns (500 VDC, 30 s). Both layers were wound continuously, with the conductor passing through a layer jump that allowed transition from the inner to the outer former without interruption. At the completion of each layer, electrical insulation was applied around the former. This insulation consisted of multiple layers of 45 mm-wide glass fibre tape wrapped with a 50% and 25% overlap on the inner and the outer curvature respectively. For the outer former, an additional layer of polyimide was added as electrical insulation against the earthed mechanical shell (see Fig. 3). The use of composite fibreglass tape ensures complete coverage with polyimide while maintaining flow paths for epoxy impregnation.

C. Former insertion

Between the winding of the inner and outer layers, a critical step is the insertion of the outer former around the inner one. This operation is particularly delicate, as the nominal radial gap between the formers is only 0.2 mm, and the curved geometry provides very limited degrees of freedom for alignment and movement.

Fig. 4. Slowly sliding the outer former over the inner former.

This was achieved through the use of tapered formers: the formers have a diameter that is 10 mm smaller on one end compared to the other. This taper allows for a less constrained insertion over most of the length, with tight fitting occurring only at the final stage. To match the taper, the coils are also wound with a tapered profile, and the turn pitch is adjusted along the length to preserve a flat magnetic field. Insertion was carried out using custom tooling in which the outer former rested on 3 skates mounted on ball wheels, while the inner former remained fixed. First a set of specific flanges, fixed to the formers, with reference surfaces was used to precisely align and level the formers together by adjusting the height of each skate. Then the outer former was guided into place along a curved rail that followed the magnet's bending radius (see Fig. 4). The combination of the tapered geometry and dedicated tooling significantly eased the insertion process and ensured proper assembly without damaging neither the windings nor the insulation.

D. Impregnation

The coil is encapsulated within a clamshell mechanical structure (see Fig. 5), with a nominal radial gap of 0.2 mm between the outer former and the shell. The complete assembly then undergoes vacuum pressure impregnation (VPI) to produce a rigid, monolithic conductor block. This process is essential to minimise conductor motion within the groove, which could degrade the magnetic field quality. The clamshell is designed to function as a sealed mould and remains closed after impregnation to ensure complete filling of all voids. The epoxy resin used is the usual recipe for CTD-101 K commonly used in accelerator magnets, with an innovative addition of DY-040 [15]. This flexibiliser improves fracture toughness at cryogenic temperatures by approximately 50%, thereby reducing the risk of cracking. Previous cold tests on subscale models have demonstrated the good training performances of this impregnation system as the magnets reached their short sample limit in few quenches [11]. Post-mortem metallographic analysis have supported these results emphasising the quality of the impregnation and the resin after the tests. A total of 11 kg of resin was injected at 60°C

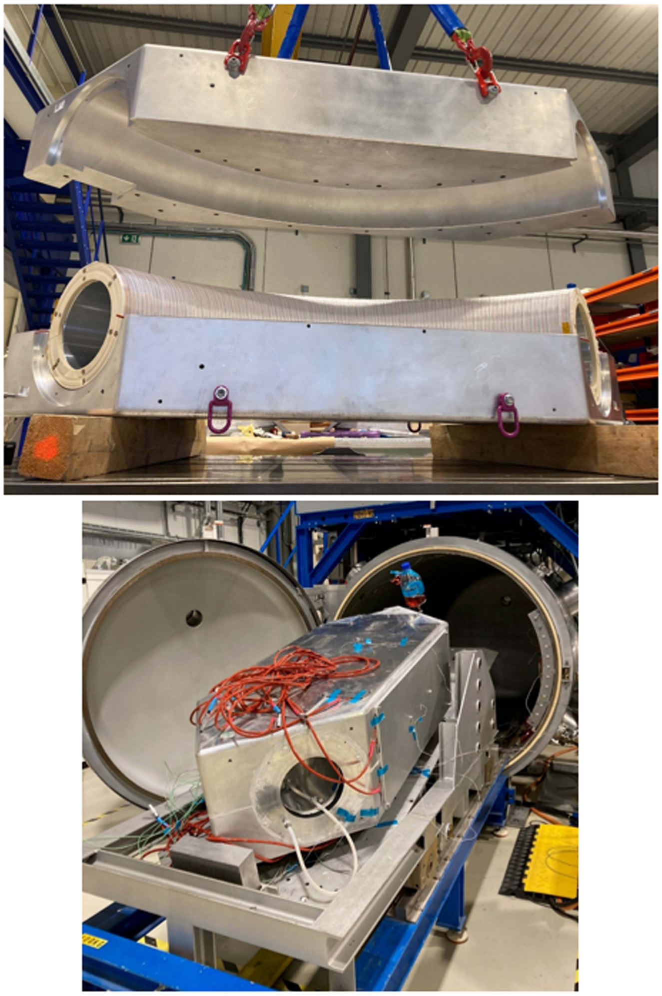

Fig. 5. Closing of the top part of the clamshell (top). Fusillo magnet in front of the vacuum chamber, ready for impregnation (bottom).

over a period of 3 hours. The polymerisation cycle consisted of 24 hours at 80°C, followed by 5 hours at 110°C, and finally 16 hours at 125°C. The magnet was heated using a set of eight resistive heating plates surrounding the structure (see Fig. 5).

E. Splicing

The final operation after impregnation is the electrical connection of the 140 wire ends in series, achieved through 69 splices. The splice box (see Fig. 6) is located outside the mechanical structure and is therefore not impregnated, allowing access to the splices for repair in case of failure. An ultrasonic welding technique—based on the application of high-frequency vibrations combined with pressure to locally melt the copper—was specifically developed for this application. This method produces highly reproducible and mechanically robust splices, in which the Nb-Ti filaments of both wires are brought into near contact: 45±20 μm as measured on metallographic cross-sections (Fig. 6). Electrical resistance measurements conducted at cryogenic temperatures on 1 cm-long test samples yielded a resistance of 3.6±0.1 nΩ per splice suggesting a resistance of

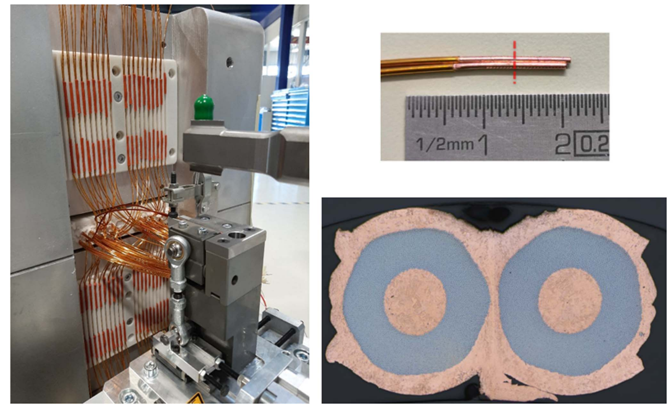

Fig. 6. View of the splice box located above and below the cable exit with the ultrasonic welding device in front (left). Microscopic view of a splice (top right) cross section where the Nb-Ti mutlifilamentary area (grey) are almost in contact (bottom right).

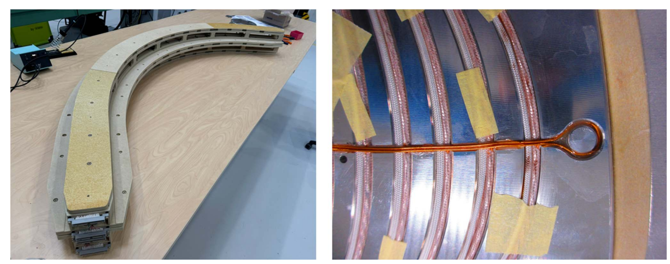

Fig. 7. View of the assembled curved magnetometer (left). Close-up on the FQPC crossings and loop turn at the end of the 65 turns (right).

1.2±0.1 nΩ on the final 3 cm-long splices of the demonstrator magnet.

IV. Instrumentation

Local magnetic field measurements are carried out using an array of uniformly distributed conduction coils positioned along the curvature of the aperture. In addition, the magnetometer (see Fig. 7) is instrumented with cryogenic Hall sensors, which are cross-calibrated *in situ* using the induction coils system, as described in [16]. The magnetometer assembly consists of three PCB layers: one situated at the magnetic mid-plane and two symmetrically placed at ±72.7 mm. These PCBs are rigidly supported by a fibreglass structure installed within the magnet aperture whose mechanical description as well as test results on subscale models are given in [11].

In addition to magnetic measurements, several other types of instrumentation have been implemented on the demonstrator. Distributed fibre-optic sensing (DFOS) is employed to monitor deformation along the conductor. This deformation, resulting from either temperature variations or mechanical strain during powering, has already been successfully observed using this technique in previous studies [17]. In the Fusillo magnet, the optical fibres are first braided with a thick fibreglass layer before being co-wound with the conductor, positioned at the top and bottom corners of the groove (see Fig. 1). A fast quench propagation conductor (FQPC) system—an innovative quench protection method developed specifically for CCT magnets—is also implemented. It consists of a superconducting wire perpendicular in with the winding turns to facilitate rapid quench propagation between them [18] (see Fig. 7). This installation represents the first large-scale demonstration of FQPC in a CCT magnet. Finally, acoustic sensors are installed on both the shell and the formers to detect and analyse sound signatures associated with quench events or their precursors.

V. Conclusion

We have designed and manufactured a curved CCT dipole magnet at CERN, generating 3 T at 4.5 K in a 236 mm aperture. The rope cable, consisting of seven insulated Nb-Ti strands, has been produced with a novel extruded TPI insulation on each strand. All fabrication steps — from producing the curved formers by joining three sections, to winding, impregnation, and a newly developed ultrasonically welded splicing — were completed without major issues, thanks to specific and adaptive tooling. The power tests of the magnet are scheduled for summer 2025.

Acknowledgment

The authors would like to thank: R. Ferriere for his work in drawing the CAD models and the main mechanical workshop at CERN for producing the formers; the polymer laboratory at CERN for the impregnation of the coils, and finally the mechanical measurement group for the help in implementing the optical fibres and the metallographic study of the splices.

References

[1] D. Meyer and R. Flasck, “A new configuration for a dipole magnet for use in high energy physics applications,” *Nucl. Instrum. Methods*, vol. 80, pp. 339–341, 1970, doi: 10.1016/0029-554X(70)90784-6.

[2] C. L. Goodzeit, M. J. Ball, and R. B. Meinke, “The double-helix dipole - A novel approach to accelerator magnet design,” *IEEE Trans. Appl. Supercond.*, vol. 13, no. 2, pp. 1365–1368, Jun. 2003, doi: 10.1109/TASC.2003.812672.

[3] S. Caspi et al., “Design, fabrication, and test of a superconducting dipole magnet based on tilted solenoids,” *IEEE Trans. Appl. Supercond.*, vol. 17, no. 2, pp. 2266–2269, Jun. 2007, doi: 10.1109/TASC.2007.899243.

[4] W. Wan et al., “Alternating-gradient canted cosine theta superconducting magnets for future compact proton gantries,” *Phys. Rev. Spec. Top. Accel. Beams*, vol. 18, no. 10, 2015, Art. no. 103501, doi: 10.1103/PhysRevSTAB.18.103501.

[5] L. Brouwer, A. Huggins, and W. Wan, “Design of an achromatic superconducting magnet for a proton therapy gantry,” *IEEE Trans. Appl. Supercond.*, vol. 27, no. 4, Jun. 2017, Art. no. 4400106, doi: 10.1109/TASC.2016.2628305.

[6] L. Brouwer et al., “Design and test of a curved superconducting dipole magnet for proton therapy,” *Nucl. Instrum. Methods Phys Res. A*, vol. 957, Jan. 2020, Art. no. 163414, doi: 10.1016/j.nima.2020.163414.

[7] X. Zhang et al., “Design and test of a curved canted-cosine-theta superconducting dipole magnet for next generation ion therapy,” *IEEE Trans. Appl. Supercond.*, vol. 33, no. 6, Sep. 2023, Art. no. 4401507, doi: 10.1109/TASC.2023.3272576.

[8] E. D. Matteis et al., “Straight and curved canted cosine theta superconducting dipoles for ion therapy: Comparison between various design options and technologies for ramping operation,” *IEEE Trans. Appl. Supercond.*, vol. 33, no. 5, Aug. 2023, Art. no. 4401205, doi: 10.1109/TASC.2023.3259330.

[9] G. A. Kirby et al., “Superconducting curved canted-cosine-theta (CCT) for the HIE-ISOLDE recoil separator ring at CERN,” *IEEE Trans. Appl. Supercond.*, vol. 32, no. 6, Sep. 2022, Art. no. 4004105, doi: 10.1109/TASC.2022.3158332.

[10] G. A. Kirby et al., “Hi-lumi LHC twin aperture orbit correctors magnet system optimisation,” *IEEE Trans. Appl. Supercond.*, vol. 27, no. 4, Jun. 2017, Art. no. 4002805, doi: 10.1109/TASC.2016.2633424.

[11] A. Haziot et al., “Curved-canted-Cosine-Theta (CCCT) dipole prototype development at CERN,” *IEEE Trans. Appl. Supercond.*, vol. 34, no. 5, Aug. 2024, Art. no 4002608, doi: 10.1109/TASC.2024.es3353149.

[12] M. Wozniak et al., “Quench protection of Fusillo subscale curved CCT magnet,” *IEEE Trans. Appl. Supercond.*, vol. 34, no. 5, Aug. 2024, Art. no. 4702805, doi: 10.1109/TASC.2024.3355358.

[13] M. Wozniak et al., “Quench protection of the Fusillo demonstrator curved CCT magnet,” *IEEE Trans. Appl. Supercond.*, vol. 35, no. 2, Aug. 2025, Art. no. 4902006, doi: 10.1109/TASC.2025.3539601.

[14] M. Wozniak et al., “Transient behavior of the second Fusillo subscale curved CCT magnet,” *IEEE Trans. Appl. Supercond.*, vol. 35, no. 5, Aug. 2025, Art. no. 4902206, doi: 10.1109/TASC.2025.3540828.

[15] A. Gaarud et al., “Fracture toughness, radiation hardness, and processibility of polymers for superconducting magnets,” *Polymers*, vol. 16, no. 9, May 2024, Art. no. 1287, doi: 10.3390/polym16091287.

[16] C. Petrone et al., “Measurement and analysis of the dynamic effects in a HTS dipole magnet,” *IEEE Trans. Appl. Supercond.*, vol. 28, no. 4, Jun. 2018, Art. no. 4604404, doi: 10.1109/TASC.2018.2801325.

[17] L. Luo et al., “Distributed fiber-optic sensing in a subscale high-temperature superconducting dipole magnet,” *Supercond. Sci. Technol.*, vol. 38, no. 3, Mar. 2025, Art. no. 35029, doi: 10.1088/1361-6668/adba98.

[18] M. Wozniak, E. Ravaioli, and A. Verweij, “Fast quench propagation conductor for protecting Canted Cos-Theta magnets,” *IEEE Trans. Appl. Supercond.*, vol. 33, no. 5, Aug. 2023, Art. no. 4701705, doi: 10.1109/TASC.2023.3247997.